

Asymmetric magnetism at the interfaces of MgO/FeCoB bilayers by exchanging the order of MgO and FeCoB

Md. Shahid Jamal¹, Sadhana Singh², Arun Singh Dev¹, Neha Gupta³, Pooja Gupta^{3,4}, Mukul Gupta¹, Olaf Leupold⁵, Ilya Sergueev⁵, V. R. Reddy¹, Dileep Kumar^{1,*}

1. UGC-DAE Consortium for Scientific Research, Indore, India.
2. IIT Hyderabad, Academic Block B-216, Kandi, Sangareddy, 502285, India
3. Raja Ramanna Centre for Advanced Technology, Indore 452013, India.
4. HBNI, Training School Complex, Anushakti Nagar, Mumbai 400094, India.
5. Deutsches Elektronen-Synchrotron DESY, Notkestraße 85, 22607 Hamburg, Germany.

*Email: dkumar@csr.res.in

Abstract:

Interfaces in FeCoB/MgO/FeCoB magnetic tunnel junction play a vital role in controlling their magnetic and transport properties for various applications in spintronics and magnetic recording media. In this work, interface structures of a few nm thick FeCoB layer in FeCoB/MgO and MgO/FeCoB bilayers are comprehensively studied using x-ray standing waves (XSW) generated by depositing bilayers between Pt waveguide structures. High interface selectivity of nuclear resonance scattering (NRS) under the XSW technique allowed to measure structure and magnetism at the two interfaces, namely FeCoB-on-MgO and MgO-on-FeCoB, yielding an interesting result that electron density and hyperfine fields are not symmetric at both interfaces. The formation of a high-density FeCoB layer at the MgO/FeCoB (FeCoB-on-MgO) interface with an increased hyperfine field (~34.65 T) is attributed to the increasing volume of FeCo at the interface due to boron diffusion from ⁵⁷FeCoB to the MgO layer. Furthermore, it caused unusual angular-dependent magnetic properties in MgO/FeCoB bilayer, whereas FeCoB/MgO is magnetically isotropic. In contrast to the literature, where the unusual angular dependent in FeCoB based system is explained in terms of in-plane magnetic anisotropy, present findings attributed the same to the interlayer exchange coupling between bulk and interface layer within the FeCoB layer.

Introduction:

Magnetic tunnel junctions (MTJs) based on FeCoB as a magnetic electrode and MgO as a tunneling barrier gained much attention because of their applications in random access memories and as a sensor in magnetic disc drives¹⁻³. High TMR ratio obtained in the in-plane magnetized MTJs (i-MTJs) with CoFeB/MgO/CoFeB structures^{4,5}. Despite the high TMR ratios, these devices suffer from low switching efficiency, thermal stability, and storage density. The discovery of inter-facial perpendicular magnetic anisotropy (PMA) in such a structure is

an outstanding achievement, which possesses a high TMR ratio, relatively small spin-transfer torque (STT) switching current, and low magnetic damping⁴⁻⁷.

In these systems, interfaces play a vital role in deciding the magnetic anisotropy and TMR ratio.^{5,8} Recently, amorphous FeCoB and MgO interfaces have been responsible for unusual two-step hysteresis loops with higher coercivity near the magnetic hard axis⁹. The mechanism for such magnetism has been widely debated, with most commonly suggested mechanisms such as bond-oriented anisotropy (BOA)¹⁰ and pair-ordering anisotropy (POA).^{9,11} Recently, boron diffusion at the interface^{9,12,13} has been found to be responsible for a stress-induced uniaxial magnetic anisotropy in the boron deficient FeCoB interface layer superimposed with the isotropic bulk FeCoB layer, and it creates unusual step hysteresis loop in the system. The role of interlayer exchange coupling between both layers is determined by separating magnetic contributions by fitting hysteresis loops with an adequate mathematical function⁹. In view of the facts, considerable temperature-dependent studies in the literature are also done to study interface magnetism and its role in optimizing the magnetic and transport properties of the multilayer system^{5,14}. It has been established that with increasing temperature, nanocrystallization of FeCo starts at the interfaces due to the boron diffusion.^{15,16} Unfortunately, most studies provided average information on all phenomena irrespective of the individual interfaces. In the recent past, there have been several studies where exchange in the order of ferromagnetic-non-magnetic layers is found responsible for the drastic change in the interface structure¹⁷. Namely, in the case of the Fe/Cr(Tb) multilayer, it is found that the root mean square (RMS) roughness of the two interfaces Fe-on-Tb(Cr) and Tb(Cr)-on-Fe are not equal.¹⁷ Similar to the above Fe/Cr(Tb) multilayer, Wenbin Li et al. used x-ray reflectivity (XRR) and x-ray fluorescence (XRF) techniques under x-ray standing waves (XSW) produced by periodic multilayers to explain the asymmetry in the Ti/Ni/Ti trilayer.¹⁸ They observed that the roughness of the Ti-on-Ni interface is 0.64 nm, and that of the Ni-on-Ti interface is 0.40 nm. Sagarika Nayak et al. studied the Fe/NiFe bilayer system by alternating the order of the magnetic layers by polarized neutron reflectivity (PNR).¹⁹ They found that the interfacial magnetic moment increased by almost 18% when the NiFe layer was grown over the Fe layer. A considerable amount of studies have also been put into optimizing the CoFeB/MgO interface also to improve performance. However, despite the substantial technological importance of FeCoB and MgO-based systems, no study is available in the literature where special attention

has been paid to understanding the interfaces (exchanging the order of ferromagnetic layer) to understand the unusual magnetization reversal in FeCoB and MgO-based systems.

Interface-resolved magnetic information of FeCoB-on-MgO or MgO-on-FeCoB interfaces is essentially required to get genuine information about these structures. The main difficulty is to perform depth-resolved magnetic properties or magnetism from the interface, independently from the bulk layer. Various lab-based techniques, such as superconducting quantum interface devices²⁰, magneto-optic Kerr effect (MOKE)^{7,21}, vibrating sample magnetometer²², and nuclear magnetic resonance, are available²³. These techniques, unfortunately, give average information about the magnetic layer and do not have sufficient depth resolutions or fail to probe the true interfaces. Conversion electron Mossbauer spectroscopy (CEMS)²⁴, PNR²⁵, and x-ray magnetic circular dichroism²⁶ are considered more informative and powerful methods to analyze interface magnetism. However, each technique has its advantages and disadvantages²⁷, which primarily depend on the sample size, structure, and nature of magnetic studies. For example, in the case of the CEMS technique, depth selectivity can be achieved with a thin probe resonant layer embedded at a definite depth.²⁷⁻²⁹ To study interface magnetism, a set of samples need to be prepared with a probe resonant layer (⁵⁷Fe) at different depth positions. However, full reproducibility is difficult in separate depositions. In the case of PNR, the relatively very long measurement time (several hours) due to reduced scatters per unit volume requires a relatively big sample size to have sufficient neutron scattering from the interface.³⁰ Nowadays, the third-generation synchrotron radiation source-based grazing incident nuclear resonance scattering (GINRS) technique is a powerful method³¹⁻³³. High scattering yield and isotope selectivity make it possible to measure the magnetic depth profile of magnetic thin films and multilayers. The proximity magnetism of the surface and interfaces can be obtained precisely using isotope material within a reasonable time, even from a fraction of a monolayer.

In the present case, an attempt has been made to explore the unusual magnetic properties in FeCoB and MgO-based systems and their correlation with the interface in FeCoB/MgO and MgO/FeCoB bilayer structures. Samples are prepared by enriching the FeCoB layer with a ⁵⁷Fe isotope to study interface magnetism using the isotope selective GINRS technique. To enhance scattering resonance yield from the ⁵⁷Fe, GINRS measurements are performed under XSW conditions. For this purpose, ⁵⁷FeCoB/MgO and MgO/⁵⁷FeCoB bilayers are deposited in the Pt

waveguide structure, and interface selectivity was achieved due to the crossing of XSW antinodes with the interface at an appropriate x-rays incident angle. Prior to GINRS measurements, the correct position of the antinode (inside the cavity $^{57}\text{FeCoB/MgO}$ and $\text{MgO}/^{57}\text{FeCoB}$) with respect to the $^{57}\text{FeCoB}$ layer is monitored by performing nuclear and electronic Fe fluorescence under XSW. The combined study of MOKE and GINRS with x-ray fluorescence (XRF) has been adopted to develop a better understanding of the FeCoB/MgO interface (by exchanging the order of MgO and FeCoB layers), which could be helpful in the development of FeCoB/MgO based MTJs.

2. Experimental

A set of six bilayer samples, $\text{FeCoB}(x)\text{-on-MgO}(6.5\text{ nm})$ and $\text{MgO}(6.5\text{ nm})\text{-on-FeCoB}(x)$, where $x = 4, 10$ and 14 nm , were prepared. For GINRS measurements, the FeCoB layers were deposited by sputtering a ^{57}Fe enriched ($\sim 99.999\%$ pure) target with the composition $\text{Fe}_{43}\text{Co}_{40}\text{B}_{17}$. High-dense Pt layers of 30 nm and 2.5 nm are used respectively as a buffer and capping to protect the surface and to generate XSW between Pt waveguide structures. All samples were deposited using an Ar ion beam sputtering technique on $\text{Si}(001)$ substrate at room temperature at a base pressure of about 1×10^{-6} torr. The chamber was flushed with pure Ar a few times before deposition to reduce the oxygen and water vapor contamination. The targets were kept such that the incident beam makes 45° to the target normal. The substrate and target were kept parallel at 15 cm apart. Each target was pre-sputtered for 2 minutes to remove the contamination from the target surface. During deposition, the working pressure was maintained at about 1×10^{-3} torr by keeping the Ar gas flow rate at 5 sccm . Respective deposition rates in all the bilayers for Pt, FeCoB, and MgO were $0.7, 0.4,$ and 0.3 \AA/s . Both sets of samples are deposited under identical conditions, ensuring chemical homogeneity and consistency in composition. The final sample structures $\text{Si}_{\text{sub}}/\text{Pt}(30)/\text{MgO}(6.5)/^{57}\text{FeCoB}(x)/\text{Pt}(2.5)$ and $\text{Si}_{\text{sub}}/\text{Pt}(30)/^{57}\text{FeCoB}(x)/\text{MgO}(6.5)/\text{Pt}(2.5)$ are designated as M-FCB_x and FCB_x-M, respectively, further in the manuscript.

X-ray reflectivity (XRR) measurements have been performed on both samples by using a diffractometer (model D5000 of Siemens) with $\text{Cu-K}\alpha$ radiation to get information about the layer thicknesses and rms interface roughnesses. MOKE measurements were performed to get magnetic information from the bilayer structures. The ^{57}Fe nuclei in the samples were excited by a photon beam with an energy of 14.4 keV for the GINRS and XRF measurements, which were conducted

at the nuclear resonance beamline P01 at PETRA III, Hamburg, Germany.^{27,32} The synchrotron operated in the 40-bunch mode with a bunch separation of 192 ns. An avalanche photodiode detector was used for GINRS measurement, having a time resolution of ~ 1 ns, while a silicon drift detector was used for XRF measurement.

3. Results and discussion

Figure 1 (a & c) gives the x-ray reflectivity of both sets of multilayers (M-FCB_x and FCB_x-M; x = 4, 10 and 14 nm), as a function of momentum transfer vector $q = 4\pi\sin\theta/\lambda$, where θ being the angle of incidence. Reflectivity data has been fitted using Parratt's formalism³⁴ to get the thickness (d) and electron density (ρ) of the individual layers in the multilayer. The continuous curve gives the fitting of the reflectivity data yielding the multilayer structure with fitting parameters shown in table 1.

Table1: XRR fitting parameters such as; thickness and electronic density for both sets of samples M-FCB_x and FCB_x-M using Parratt's formalism. The thickness of the buffer (Pt=30nm) and capping (Pt=2.5nm) layers are identical in all samples. Errors in layer thickness are ± 0.1 nm.

M-FCB_x						
Layer	d (nm)			$\rho (\times 10^{-5} \text{ \AA}^{-2})$		
	x=4	x=10	x=14	x=4	x=10	x=14
⁵⁷FeCoB_{bulk}	1.0	7.0	9.4	<u>5.24</u>	<u>5.28</u>	<u>5.26</u>
⁵⁷FeCoB_{interface}	3.0	3.0	3.0	<u>5.88</u>	<u>5.86</u>	<u>5.89</u>
MgO	6.3	6.3	6.5	3.02	3.04	3.04
FCB_x-M						
MgO	7.4	6.8	6.9	2.25	2.27	2.20
⁵⁷FeCoB	4.1	9.3	13.9	<u>5.25</u>	<u>5.28</u>	<u>5.27</u>

The corresponding scattering length density (SLD) profiles for all six samples, extracted from the fitting, are presented in Fig. 1(b & d). Interestingly, in the case of M-FCB_x samples, the best data is obtained only after adding a high-density FeCoB layer (say ⁵⁷FeCoB_{interface} layer) of about ~ 3

nm at the $^{57}\text{FeCoB}$ -on-MgO interface. The density of the $^{57}\text{FeCoB}_{\text{interface}}$ layer ($\rho \approx 5.88 \times 10^{-5} \text{ \AA}^{-2}$) is $\sim 11\%$ higher than the bulk $^{57}\text{FeCoB}_{\text{bulk}}$ layer ($\rho \approx 5.28 \times 10^{-5} \text{ \AA}^{-2}$). On the other hand, in the case of $\text{FCB}_x\text{-M}$ samples, the best fit of the XRR patterns was obtained for the uniform density of the FeCoB layer.

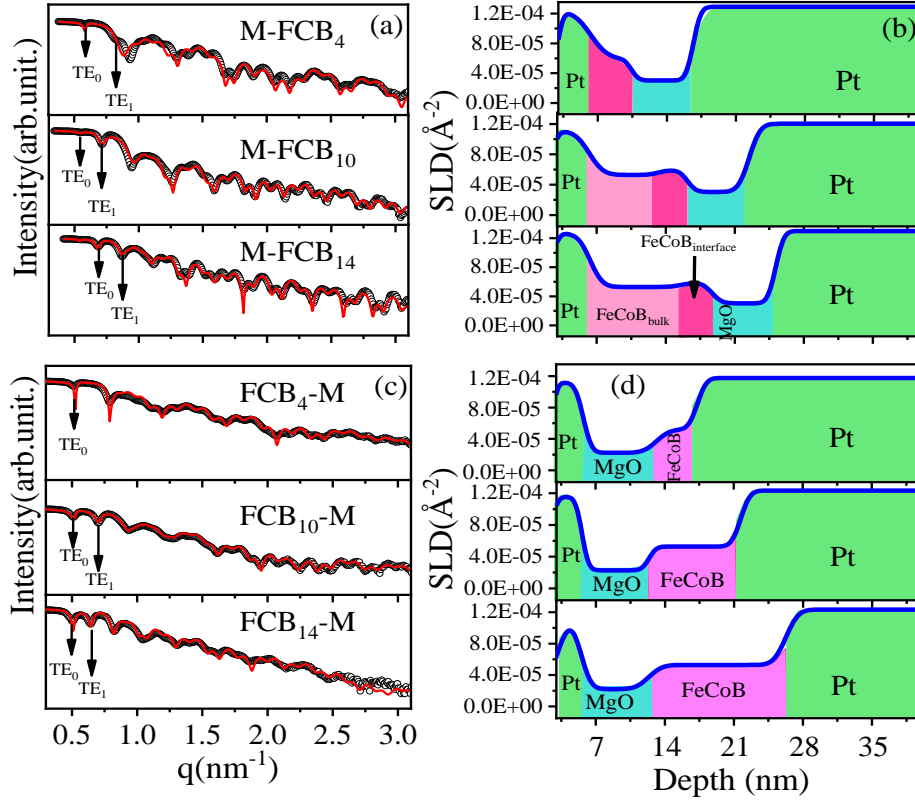


Figure 1 (a, c) X-ray reflectivity data (symbols) and corresponding best fit (solid red line) to the data for the samples M-FCB_x and $\text{FCB}_x\text{-M}$ by using Parratt's formalism, respectively. The corresponding SLD profile along with the depth of samples (b) M-FCB_x (c) and $\text{FCB}_x\text{-M}$.

It is important to note that, in all sets of samples, sharp dips in XRR below the critical angle of Pt ($q < 0.8 \text{ nm}^{-1}$) confirm the formation of standing wave modes in the cavity of the waveguide structure.^{17,35,36} This aspect will be discussed later in the manuscript.

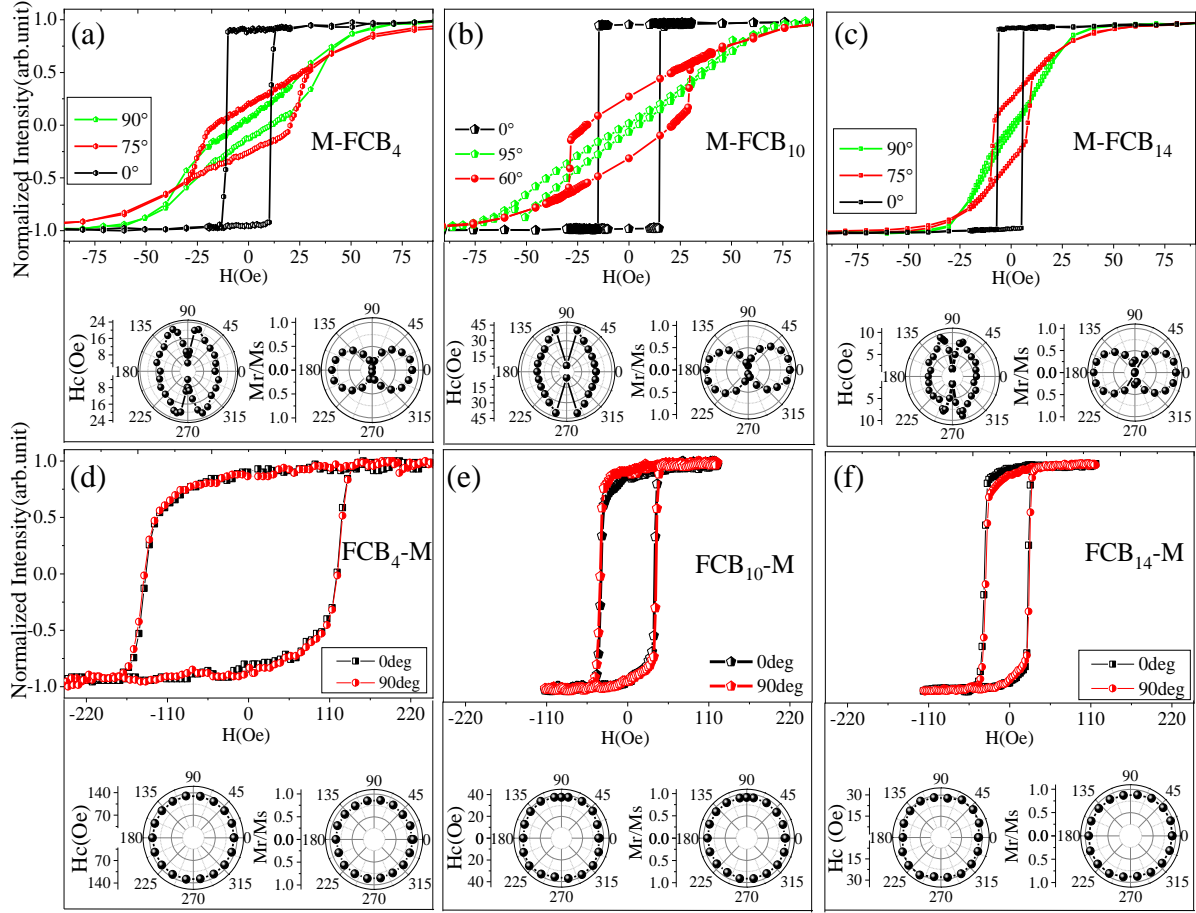


Figure 2. Representative MOKE loops with some azimuthal angles and the corresponding Hc and Mr/Ms plots as a function of azimuthal angle for samples (a-c) M-FCB_x and (d-f) FCB_x-M.

Hysteresis loops of both sets of bilayer samples were collected as a function of azimuthal angle (ϕ) using MOKE. Figure 2 (a, b, & c) shows some representative hysteresis loops collected along $\phi = 0^\circ, 75^\circ,$ and 90° for samples M-FCB_{x=4, 10, 14} nm. Along $\phi = 0^\circ$ direction, the hysteresis loop is rectangular with a well-defined coercive field of $\sim 15, 15,$ & 7 Oe for $x = 4, 10,$ and 14 nm, respectively. With increasing ϕ , the rounding off of the hysteresis curve increases up to $\phi = 90^\circ$ (hard axis), indicating the increasing contribution of the rotation of domain magnetization⁹. In polar plots with increasing ϕ , coercivity (Hc) and remanence (Mr/Ms) values are presented alongside of their respective MOKE hysteresis loops shown in Fig. 2(a-c).

The dumbbell shape of the Mr/Ms plots suggests the presence of UMA in all three samples of this set.³⁷ Interestingly, the Hc increases with increasing ϕ from 0° and reaches its maximum of about $\phi = 70\text{-}85^\circ$. On the other hand, Hc drops suddenly near zero around $\phi = 90^\circ$. In conventional magnetic anisotropy systems³⁷, which follow the Stoner-Wohlfarth model⁹, Hc is always higher

along the easy axis than in the other directions. Unexpected H_c behavior in the present case may be related to the high-density layer at the interface.

Contrary to this, as shown in figure 2 (d, e, & f), the hysteresis loops are almost independent of the azimuthal direction for all samples of set FCB_x-M. On the other hand, H_c is found sensitive to the increasing thickness of the ⁵⁷FeCoB layer. H_c and M_r/M_s vs ϕ are presented in polar plots along with their corresponding MOKE hysteresis loops in Fig. 2 (d-f). H_c reaches from 132 Oe to 28 Oe with increasing thickness of ⁵⁷FeCoB from 4 nm to 14 nm. Full range angular variation of H_c and M_r/M_s as a function of ϕ shows the absence of UMA.

To understand the origin of the unusual angular dependence of H_c in M-FCB_x series, H_c/H_a vs ϕ (H_c/H_a curve) are plotted in Fig. 3 (a-c). Here, H_a is the anisotropic field constant, defined as the variation in the magnetic fields needed to reach saturation magnetization along the easy ($\theta = 0^\circ$) and hard ($\theta = 90^\circ$) magnetization direction.³⁸ It can be obtained with the help of easy and hard hysteresis loops using the following relation-

$$H_a = H_{\text{sat}}(\text{hard loop}) - H_{\text{sat}}(\text{easy loop}) \quad 1$$

Where H_{sat} is the saturation field, H_a is calculated 58, 66, and 35 Oe, respectively, for $x = 4, 10,$ and 14 nm samples in series M-FCB_x (see Fig. 2a to 2c) H_c/H_a curve compared with available models for magnetic anisotropy such as Stoner-Wohlfarth (SW) model³⁹, Kondorsky model⁴⁰, and two-phase model⁴¹.

It is to be noted that for uniaxial systems in which the reversal mechanism is controlled by domain wall depinning, the H_c is in its simplest form described by the Kondorsky relation $H_c^{\text{Kon}} = H_c(0)/\cos\phi$.⁴⁰ It gives a monotonic increase in H_c as a function of the angle from 0° to 90° ; hence, it can not match the observed H_c variation in the present case due to divergence at 90° .⁴²

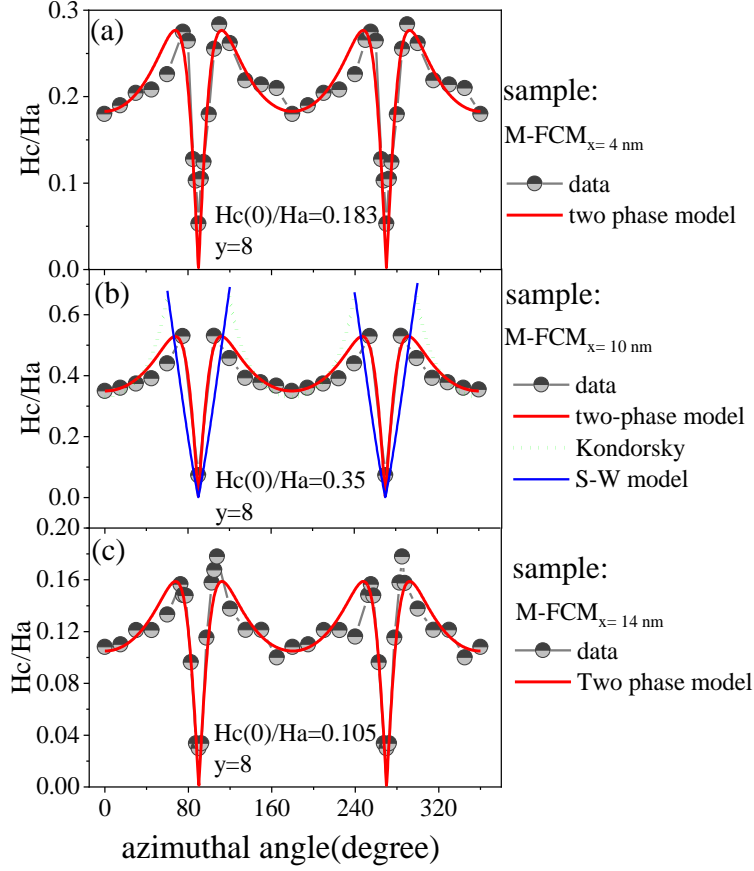


Figure 3. (a-c) H_c/H_a variation as a function of azimuthal angle (ϕ) for series M-FCB_x for $x = 4, 10,$ and 14 nm, respectively and fitted with Eq. (2) for all samples. In (b), the fittings of the H_c/H_a vs ϕ , in the limited range of ϕ using Kondorsky (dashed green line) and S-W (solid blue line) models, are also shown, together with the fitting of the H_c/H_a vs ϕ in the entire range of ϕ (solid red line) using two phase model.

Stoner-Wohlfarth (S-W) model, which is based on coherent rotation, H_c is a monotonously decreasing function of ϕ ; therefore, it will also not explain H_c variation³⁹. To demonstrate the same, Fig. 3(b) gives the fitting of the H_c curve for the “M-FCM₁₀” sample using the SW (blue line) and Kondorsky (dashed green line) models separately. But neither of the two models fit the data correctly.

In the case of the two-phase model, the magnetization reversal mechanism combines the domain wall nucleation (Kondorsky model) and domain rotation (S-W model)^{41–44}. According to this model, the H_c variation as a function of ϕ is expressed as⁴⁴

$$H_c(\phi) = \frac{H_c(0) (N_N + N_x) \cos \phi}{N_z \sin^2 \phi + (N_N + N_x) \cos^2 \phi} \quad 2$$

For $\phi = 0^\circ$, applied magnetic field along the easy axis direction, the coercive field is equal to the nucleation field $H_c(0)$. The N_x and N_z are the demagnetizing factors in the x-axis and z-axis direction, respectively (x-axis corresponding to the easy axis of magnetization). N_N is the effective demagnetization factor defined in terms of anisotropy field H_a and saturation magnetization M_s by the equation $N_N = H_a/M_s$. The parameter $y = (N_x + N_N)/N_z$ is a measure of anisotropy strength, and it can be obtained by fitting the above equation. For a large value of y , the above equation reduces to the original Kondorsky relation $H_c^{Kon} = H_c(0)/\cos\phi^{40}$. The above equation predicts a maximum value of H_c close to the hard axis direction ($70-85^\circ$) and zero for $\phi = 90^\circ$. Hence, the divergence in the hard axis direction of the Kondorsky relation is removed and replaced with a minimum. As shown in Fig. 3(a-c), the H_c/H_a variation is reasonably fitted (continuous red line) using a two-phase model for a whole angle ϕ with equation 2, indicating the validity of the two-phase model in explaining the magnetization reversal.

To further understand the unusual magnetization reversal precisely, interface resolved magnetism of two samples for $x = 10$ nm from both series (M-FCM₁₀ and FCM₁₀-M) is studied using GINRS under XSW conditions. Here, XSW is generated between the high-density Pt layers (cavity) due to the interference between the incident and reflected plane waves when x-rays are incident below a critical angle (θ_c) of Pt. Rearrangement of the electric field intensity (EFI) in the cavity takes place such that several transverse electric modes are excited at fixed angle θ_m .³⁵

$$\theta_m = \frac{(m+1)\lambda}{2Wn} \quad 3$$

where λ , W , n , and m are the wavelength of x-rays, the thickness of the cavity, the refractive index, and the order of the mode, respectively. The schematic of XSW modes inside the cavity is shown in Fig. 4.

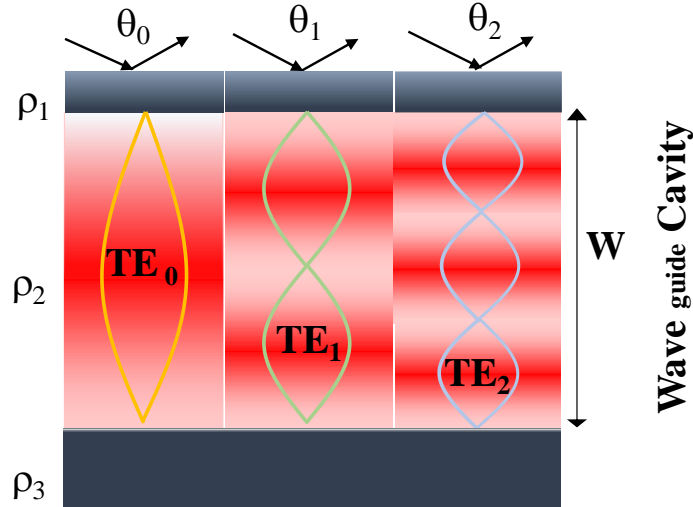


Figure 4. Schematic representation of symmetric Pt waveguide structure. W is the thickness of the cavity. TE_0 , TE_1 , and TE_2 are the transverse waveguide modes formed inside the cavity for $\rho_1 > \rho_2$ and $\rho_3 \geq \rho_1$, where ρ_1 , ρ_2 , and ρ_3 are the densities of top high-density Pt layer, cavity, and bottom Pt layer, respectively.

The formation of the EFI with an increasing incident angle inside the $^{57}\text{FeCoB/MgO}$ cavity is simulated using Parratt's recursion algorithm³⁴ for samples $\text{FCB}_{10}\text{-M}$ and $\text{FCB}_{10}\text{-M}$ by taking an incident x-ray of energy 14.4 keV. As clear from the simulated contour plot in Fig. 5 (a & c), the resonance enhancement of the x-ray intensity inside the cavity occurs. The well-localized XSW antinodes corresponding to TE_0 , TE_1 , and TE_2 modes are visible in both the samples at a fixed value of $q_0 = 0.56$, $q_1 = 0.72$, & $q_2 = 0.96 \text{ nm}^{-1}$ (for $\text{M-}^{57}\text{FCB}_{10}$) and $q_0 = 0.55$ & $q_1 = 0.73 \text{ nm}^{-1}$ (for $^{57}\text{FCB}_{10}\text{-M}$), respectively. To establish how such a structure can improve the depth sensitivity from the $^{57}\text{FeCoB}$ layer, XRF and nuclear resonance reflectivity (NRR) as a function of $q = 4\pi \sin \theta/\lambda$, is measured for both the samples and shown in Fig. 5(b & d) the contour plots. It is clear that the XRF and NRR spectrum consist of two peaks corresponding to the dips in XRR in both the samples at a fixed value of $q_0 = 0.56$ & $q_1 = 0.72 \text{ nm}^{-1}$ for M-FCB_{10} and $q_0 = 0.55$ & $q_1 = 0.73 \text{ nm}^{-1}$ for $^{57}\text{FCB}_{10}\text{-M}$, respectively. The intensity of NRR from the thin layer is proportional to the fourth power of the standing wave amplitude compared to the square dependence of XRF.⁴⁵ Hence, the relative peak intensities for XRF and NRR are different.

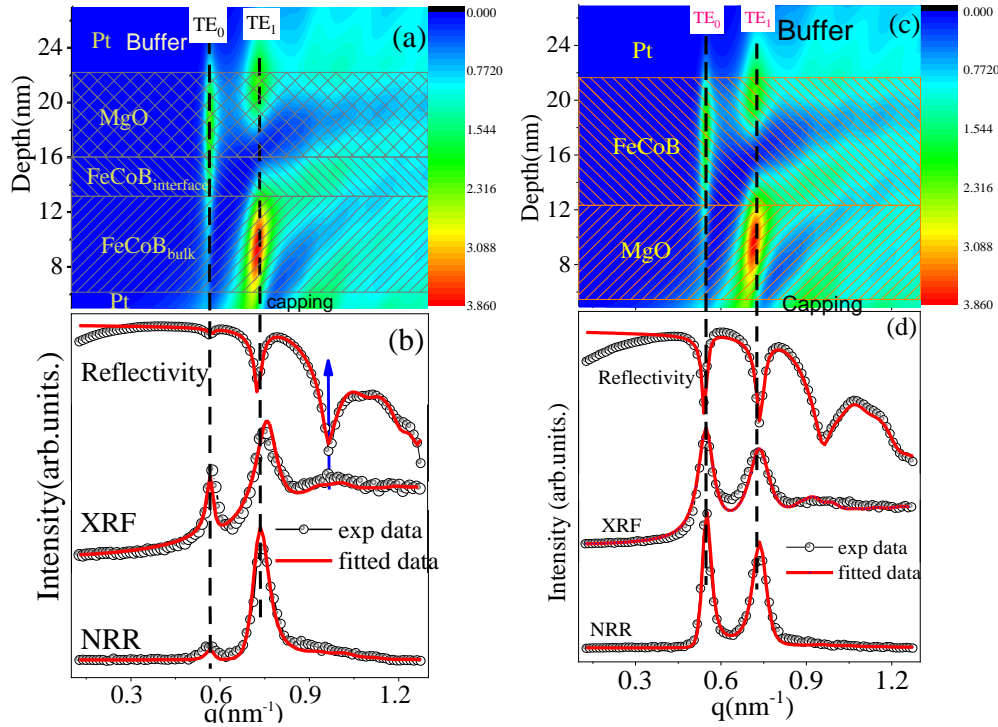


Figure 5. The angular depth distribution of simulated intensity and fitted XRR, XRF and NRR pattern for sample M-FCB₁₀ (a&b) and FCB₁₀-M (c&d). Position of the FeCoB and MgO layers are marked in the contour plot.

The origin of such peaks can be understood with the help of EFI in the trilayer, as shown in contour plots (Fig. 5 a & 5c). In the case of sample “M-FCB₁₀”, for $q_0 \approx 0.56 \text{ nm}^{-1}$, TE₀ antinode overlaps with mainly ⁵⁷FeCoB-on-MgO interface layer (high-density layer), giving rise to the peak in the XRF and NRR at $q_0 \approx 0.56 \text{ nm}^{-1}$. However, the increase in q , TE₁ antinode overlaps preferentially with the ⁵⁷FeCoB_{bulk} layer at $q_1 \approx 0.72 \text{ nm}^{-1}$ and gives rise to the related peaks in XRF and NRR. For sample “FCB₁₀-M”, at $q_0 \approx 0.55$, the TE₀ antinode fully overlaps with the whole ⁵⁷FeCoB layer, whereas the TE₁ antinode overlaps partially with the ⁵⁷FeCoB layer at $q_1 \approx 0.73 \text{ nm}^{-1}$, giving rise to a relatively less intense peak in XRF and NRR curves compared to $q_0 \approx 0.55 \text{ nm}^{-1}$. It is clear that a small variation in the depth and electron density of either part of the ⁵⁷FeCoB layer would result in a significant variation in the relative intensities of fluorescence peaks corresponding to XSW modes.^{27,32} Therefore, the experiment performed at these q values (q_0 and q_1) will enhance the contribution from the ⁵⁷FeCoB layer (bulk and interface parts). Such enhancement in the signal becomes very important to investigate genuine properties when the probing layer is thin.

GINRS measurements were performed at $q \approx 0.56, 0.72, \text{ and } 0.96 \text{ nm}^{-1}$ for sample M-FCB₁₀ and at $q \approx 0.55 \text{ and } 0.73 \text{ nm}^{-1}$ for sample FCB₁₀-M. As we know, this technique is a time analogous to Mossbauer spectroscopy³¹ and, therefore, sensitive to the hyperfine field and spin orientations of the resonant isotope (⁵⁷Fe) in probing layer ⁵⁷FeCoB. The fitting parameters, such as the hyperfine field (Bhf), the width of hyperfine field distribution (Δ Bhf), and the direction of the magnetic hyperfine field, are utilised for the fitting. The magnetic hyperfine field direction is defined in terms of two angles, namely, angle β with respect to the surface normal and the azimuthal angle γ with respect to the direction of polarization of x-rays (Fig. 6a). Δ Bhf represents the distribution of hyperfine fields around the mean value Bhf. Oscillations in resonant count (fig. 6b and 6c) in GINRS spectra are due to the interference of electromagnetic waves emitted by different hyperfine components called quantum beats. The beating patterns in both the samples are fitted using REFTIM software⁴⁶ by considering the interface function as an “error function”.

Figure 6(b) and 6 (d) represent the fitted GINRS spectra for samples M-FCB₁₀ and FCB₁₀-M. The best fit to GINRS data is obtained by taking bilayer structure as obtained from XRR, XRF and NRR measurements. For sample M-FCB₁₀, the four multiplets 29.85, 34.65, 32.43, & 22.41 T with ($\beta, \gamma = 90^\circ, 30^\circ$) having nuclear density concentrations of about 51, 31, 15, & 3 % in full ⁵⁷FeCoB layer (including interface layer) are used and shown in fig. 6(c). It may be noted that GINRS simulated curve (dotted line) is also included in the same figure by considering the uniform ⁵⁷FeCoB layer (no interface layer). Deviation from the best fit further confirms the existence of two magnetic layers within the FeCoB layer. The cause of different Bhfs contributions in the bulk and interface parts of the ⁵⁷FeCoB layer is mainly due to the different magnetism caused by compositional differences near the interface. For sample FCB₁₀-M, the best fit to GINRS data (red lines) was obtained by taking five multiplets 29.88, 34.43, 32.45, 30.53, & 22.14 T with ($\beta, \gamma = 90^\circ, 10^\circ$) having nuclear density concentrations of about 48, 15, 16, 18, & 3 %, respectively, in whole ⁵⁷FeCoB layer as shown in Fig. 6(e). Based on the best-fitted data for both the samples, the nuclear density distribution of Bhf along the depth of sample M-FCB₁₀ and FCB₁₀-M are presented in Fig. 6(c) and (e), respectively. The pie chart shows the nuclear density percentage contributions of Bhf for both samples in Fig. 7. For the M-FCB₁₀ sample, the total Bhf contributions for interface and bulk part, namely ⁵⁷FeCoB_{bulk} and ⁵⁷FeCoB_{interface}, are separated after fitting and presented in table 2. For example, Bhf=34.65T is 31 % in the M-FeCoB₁₀ sample (see pie fig. 7), whereas 22

% of the same is at the interface layer. Similarly, it is found that Bhf of 29.85 T is present mainly with 29% in the $^{57}\text{FeCoB}_{\text{bulk}}$ layer, whereas the interface layer $^{57}\text{FeCoB}_{\text{interface}}$ contains only 22% of the part. Moreover, $^{57}\text{FeCoB}_{\text{bulk}}$ and the $^{57}\text{FeCoB}_{\text{interface}}$ layers contain 9% and 22% with Bhf of 34.25 T, respectively. The Bhf 32.43 T is almost uniformly distributed in both the layers ($^{57}\text{FeCoB}_{\text{bulk}}$:8%, $^{57}\text{FeCoB}_{\text{interface}}$:7%) while 22.41 T is present only in the $^{57}\text{FeCoB}_{\text{interface}}$ layer with 3%.

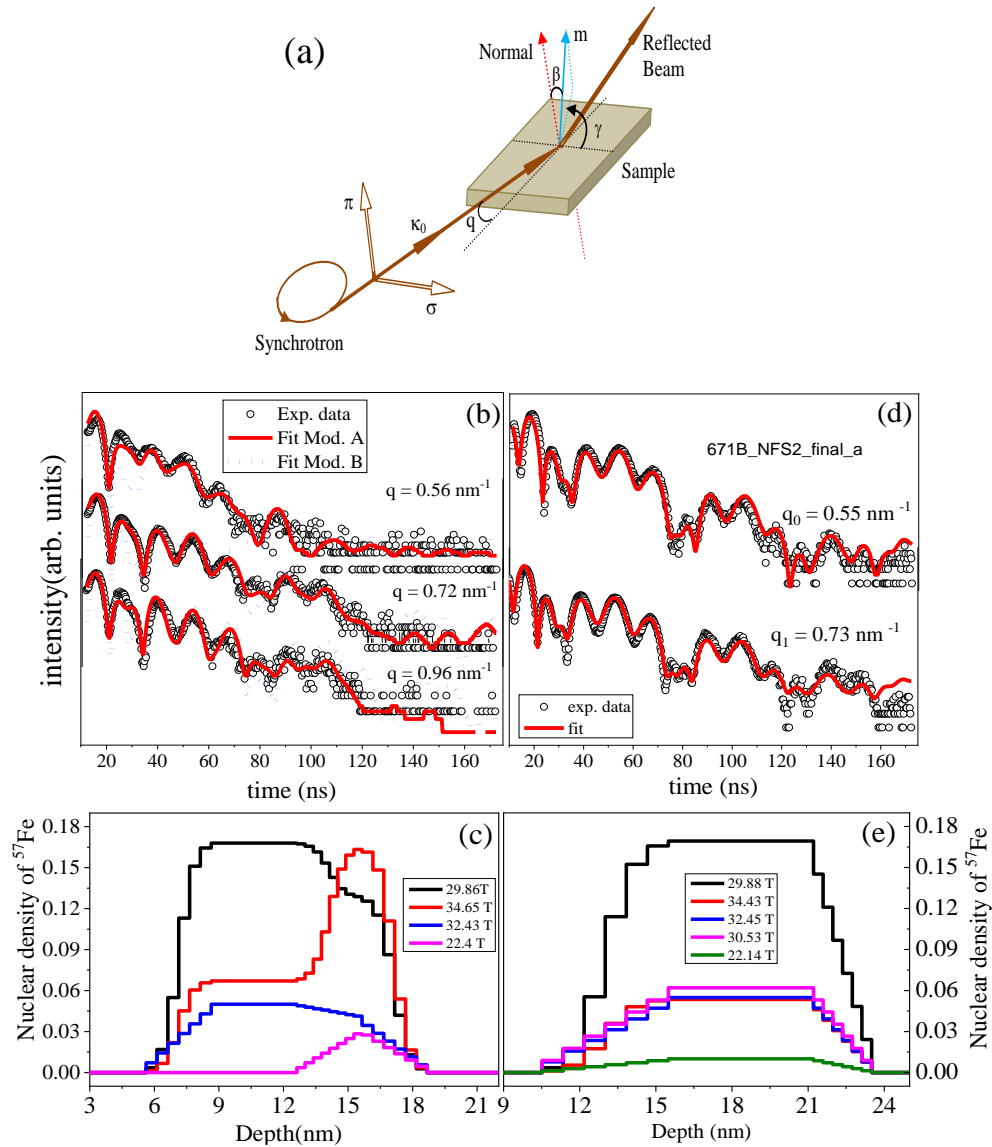


Fig. 6(a) Geometry used in the nuclear resonant scattering of synchrotron radiation from thin films and surfaces, defining the relative orientation (β , γ) of the incident wave vector k_0 to the direction of a unidirectional magnetization m of the sample. (b) & (d) GINRS data taken at different antinode positions of the standing wave, solid red lines are best fit to the data using REFTIM software. (c) & (e) represents

the multiplets density profile along with the depth for both the samples M-FCB₁₀ and FCB₁₀-M, respectively.

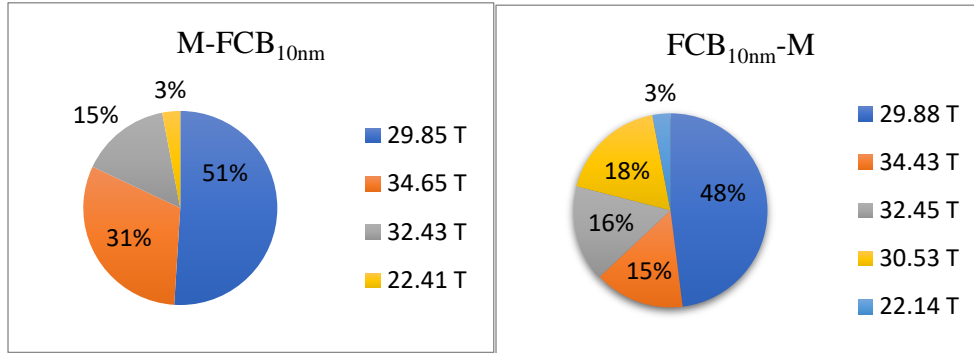


Fig. 7. Percentage contribution of Bhf in samples M-FCB₁₀ and FCB₁₀-M.

Table 2: Percentage contribution of different Bhfs in ⁵⁷FeCoB_{bulk} and ⁵⁷FeCoB_{interface} layer.

Hyperfine fields	29.85 T	34.65 T	32.43 T	22.41 T
⁵⁷ FeCoB _{bulk}	29%	9%	8%	-
⁵⁷ FeCoB _{interface}	22%	22%	7%	3%

C. E. Johnson et al. investigated the Bhf in Fe_{1-x}Co_x alloy with cobalt concentration, with the increasing amount of Co, the Bhf increases with pure iron and reaches the maximum value (36.5 T) with further addition of Co content and then decreases⁴⁷. H. P. Klein et al. studied the variation of Bhf with Co content in (Fe_{1-x}Co_x)₈₀B₂₀, and they observed that Bhf varies between 25 to 28 T⁴⁸. They also show that with a higher boron concentration, the Bhf decreases compared to the lower B content. In another study, two amorphous phases (with hyperfine fields 26.5 and 22 T) were observed in a Fe₄₀Co₄₀B₂₀ alloy sample of a thickness of 200 nm on a clean foil by DC magnetron sputtering with frequent interruption of plasma (100 times; for 30 s in every 2 nm layer) between the target and the substrate⁴⁹. It is important to note that the different percentage contribution of Bhfs in ⁵⁷FeCoB_{bulk} and ⁵⁷FeCoB_{interface} layer in the M-FCB₁₀ sample is mainly due to compositional difference. A higher contribution of 29.85 T in the ⁵⁷FeCoB_{bulk} layer suggests the domination of the ⁵⁷FeCoB phase. High ΔBhf in both the samples confirms the amorphous nature of ⁵⁷FeCoB films¹³. In the case of the M-FCB₁₀ sample, the increased contribution of 34.43 T in the

$^{57}\text{FeCoB}_{\text{interface}}$ part and decreasing contribution of 29.85 T in the $^{57}\text{FeCoB}_{\text{interface}}$ region is mainly due to FeCo phase formation caused by boron diffusion during $^{57}\text{FeCoB}$ deposition on MgO⁹.

Discussion

J. D. Burton et al. demonstrated using first-principle calculations that in the FeCoB/MgO/FeCoB MTJ, the presence of B causes the bonding of Fe-O or Co-O at the interface to be weakened by the existence of more advantageous Fe-B or Co-B bonding⁵⁰. In another study by an x-ray photoemission spectroscopy of CoFeB/MgO bilayers were observed the formation of B, Fe, and Co oxides at the CoFeB/MgO interface due to oxidation of CoFeB during MgO deposition. In contrast to the literature, they observed that the vacuum annealing reduces the Co and Fe oxides formation but forms a composite MgB_xO_y layer due to B diffusion into MgO¹⁵. Therefore, there is a contradiction regarding oxide formation at the FeCoB/MgO interface. In the present case, observation of a high-density layer at the interface negates the oxide layer formation; otherwise, a low-density layer with nonmagnetic contribution might have been observed in XRR and NRR data analysis.

It is important to note that the electronic density and Bhf of FeCo are higher than FeCoB layer^{9,47,48}. Therefore, the only possible reason for the high-density interface layer ($^{57}\text{FeCoB}_{\text{interface}}$) and increasing contribution of higher Bhf at the interface in the M-FCB₁₀ sample is the diffusion of B from the $^{57}\text{FeCoB}$ layer to the MgO layer near the interface. B migration into MgO can occur due to the higher electron affinity of Mg and O and its size which is smaller than Fe and Co. The MgO layer was deposited by the ion beam sputtering technique and has a finite probability of oxygen deficiencies^{9,51,52}. The stress in the interface layer may stabilize the stress-induced UMA in the $\text{FeCoB}_{\text{interface}}$ layer at the interface^{53,54}. Due to the lack of long-range structural order, the FeCoB layer generally does not possess UMA. The $\text{FeCoB}_{\text{bulk}}$ layer (isotropic) and $\text{FeCoB}_{\text{interface}}$ layer (anisotropic) are coupled magnetically and cause unusual angular-dependent hysteresis loops⁹.

The observed angular-dependent shapes of the hysteresis loop are further verified and understood by depositing a separate trilayer structure (Si/Co(20 nm)/Alq₃ (50 nm)/Co(20 nm) with anisotropic and isotropic Co layer in the same trilayer sample. Before this, two separate samples, Si/Co (20 nm) and Si/Alq₃(50 nm)/Co(20 nm), were deposited in identical conditions.

It was found that Co exhibits magnetic anisotropy on the Si substrate (fig. 8a), whereas Co on Alq3 is isotropic. Anisotropy in Si/Co is mainly due to the long-range stress development during film growth.^{53,54} On the other hand, these stresses are negligible or absent on the organic layer (Alq3) due to the mechanical softness of the Alq3 layer.

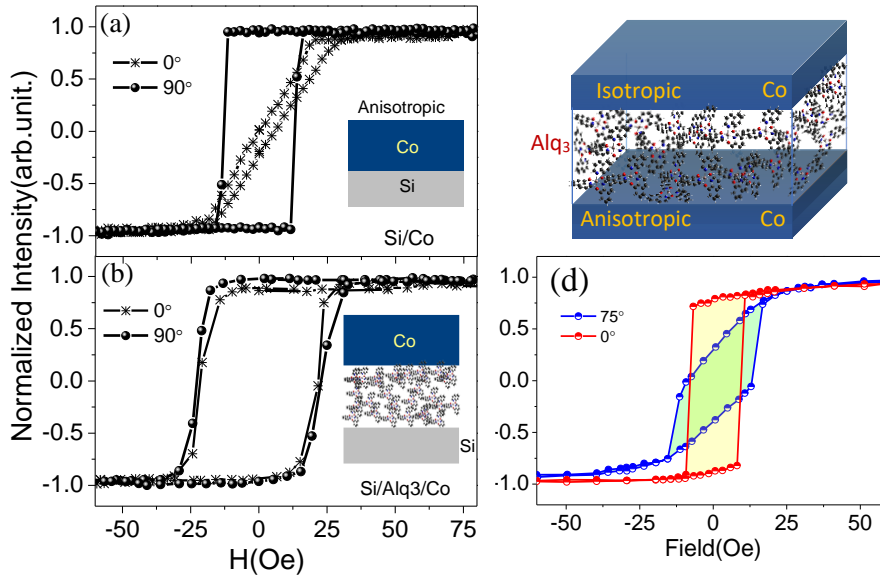


Figure 8. MOKE loops along 0° and 90° for the sample (a) Si/Co(20 nm), (b) Si/Alq₃(50 nm)/Co(20 nm), (c) schematic of combined trilayer structure Co(20nm)/Alq₃(50nm)/Co(20 nm), where top Co is isotropic, and bottom Co is anisotropic (d) MOKE loops of the trilayer along 0° and 75° .

Combining these two samples in a trilayer confirms the coexistence of anisotropic and isotropic layers in the same sample. Figure 8(d) gives MOKE loops of trilayer along its easy (0°) and near hard axis (75°) of magnetization. The hysteresis loop along 0° has $H_c \sim 8$ Oe, less than the H_c along $\sim 75^\circ$. These loops match well with the M-FCB_x bilayers in the present work. These findings further confirm and validate the model of the anisotropic interface layer in the M-FCB_x bilayer. Here, the isotropic bulk and anisotropic interface layer couples and cause unusual shapes of hysteresis loops in azimuthal angle-dependent hysteresis loops.⁹

Conclusion

The role of interface modification on the magnetization reversal of the ⁵⁷FeCoB/MgO and MgO/⁵⁷FeCoB bilayer structures have been studied by performing interface resolved GINRS and XRF measurements under the x-ray standing waves (XSW) conditions. Highly sensitive interface resolved measurements allowed to

measure structure and magnetism at the two interfaces, namely FeCoB-on-MgO and MgO-on-FeCo. The combined analysis revealed that electron density and hyperfine fields are not symmetric at both interfaces. ⁵⁷FeCoB-on-MgO bilayer exhibits UMA, while MgO-on-⁵⁷FeCoB bilayer is found magnetically isotropic. The formation of a high-density FeCoB layer at the MgO/FeCoB (FeCoB-on-MgO) interface is attributed to the increasing volume of FeCo at the interface due to boron diffusion from ⁵⁷FeCoB to the MgO layer. Furthermore, the formation of high dense layer at the interface caused unusual angular-dependent magnetic properties in MgO/FeCoB bilayer. In comparison to the literature, where the unusual angular dependent in FeCoB based system is explained in terms of in-plane magnetic anisotropy, present findings attributes the same to the interlayer exchange coupling between bulk and interface layer. The combined analysis revealed that the interchanging order of layers (⁵⁷FeCoB-on-MgO and MgO-on-⁵⁷FeCoB) plays a key role in tuning the magnetic anisotropy through interdiffusion at the interface.

Acknowledgements:

A portion of this research was carried out at the light source PETRA-III of DESY, a member of the Helmholtz Association (HGF). Financial support by the Department of Science & Technology (Government of India) (Proposal No. I-20180885) provided within the framework of the India@DESY collaboration is gratefully acknowledged.

References

- (1) Wolf, S. A.; Awschalom, D. D.; Buhrman, R. A.; Daughton, J. M.; Von Molnár, S.; Roukes, M. L.; Chtchelkanova, A. Y.; Treger, D. M. Spintronics: A Spin-Based Electronics Vision for the Future. *Science*. Knopf 2001, pp 1488–1495. <https://doi.org/10.1126/science.1065389>.
- (2) Reiss, G.; Meyners, D. Reliability of Field Programmable Magnetic Logic Gate Arrays. *Appl. Phys. Lett.* **2006**, *88* (4), 1–3. <https://doi.org/10.1063/1.2167609>.
- (3) Löhndorf, M.; Duenas, T.; Tewes, M.; Quandt, E.; Rühlig, M.; Wecker, J. Highly Sensitive Strain Sensors Based on Magnetic Tunneling Junctions. *Appl. Phys. Lett.* **2002**, *81* (2), 313–315. <https://doi.org/10.1063/1.1483123>.
- (4) Parkin, S. S. P.; Kaiser, C.; Panchula, A.; Rice, P. M.; Hughes, B.; Samant, M.; Yang, S.-H. Giant Tunneling Magnetoresistance at Room Temperature with MgO (100) Tunnel Barriers. **2004**. <https://doi.org/10.1038/nmat1256>.
- (5) Peng, S.; Zhu, D.; Zhou, J.; Zhang, B.; Cao, A.; Wang, M.; Cai, W.; Cao, K.; Zhao, W. Modulation of Heavy Metal/Ferromagnetic Metal Interface for High-Performance Spintronic Devices. *Adv. Electron. Mater.* **2019**, *5* (8), 1900134. <https://doi.org/10.1002/aelm.201900134>.

- (6) Yuasa, S.; Nagahama, T.; Fukushima, A.; Suzuki, Y.; Ando, K. Giant Room-Temperature Magnetoresistance in Single-Crystal Fe/MgO/Fe Magnetic Tunnel Junctions. **2004**. <https://doi.org/10.1038/nmat1257>.
- (7) Jamal, M. S.; Gupta, P.; Kumar, D. Preferential Alignment of Co Moments at Oxide/Co Interface in Si/Co/Co-Oxide/Cowedge/Pt Structure. *Thin Solid Films* **2020**, *709*, 138246. <https://doi.org/10.1016/j.tsf.2020.138246>.
- (8) Dieny, B.; Chshiev, M. Perpendicular Magnetic Anisotropy at Transition Metal/Oxide Interfaces and Applications. *Rev. Mod. Phys.* **2017**, *89* (2). <https://doi.org/10.1103/RevModPhys.89.025008>.
- (9) Singh, S.; Kumar, D.; Gupta, M.; Lalla, N. P. Study of Interface Induced Anisotropic Exchange Coupling in Amorphous FeCoB/MgO Bilayer. *J. Alloys Compd.* **2019**, *789*, 330–335. <https://doi.org/10.1016/j.jallcom.2019.03.025>.
- (10) Hindmarch, A. T.; Rushforth, A. W.; Campion, R. P.; Marrows, C. H.; Gallagher, B. L. Origin of In-Plane Uniaxial Magnetic Anisotropy in CoFeB Amorphous Ferromagnetic Thin Films. *Phys. Rev. B - Condens. Matter Mater. Phys.* **2011**, *83* (21), 1–4. <https://doi.org/10.1103/PhysRevB.83.212404>.
- (11) Néel, L.; Pauthenet, R.; Rimet, G.; Giron, V. S. On the Laws of Magnetization of Ferromagnetic Single Crystals and Polycrystals. Application to Uniaxial Compounds. *Cit. J. Appl. Phys.* **1960**, *31*, 27. <https://doi.org/10.1063/1.1984592>.
- (12) Jamal, M. S.; Kumar, Y.; Gupta, M.; Gupta, P.; Sergeev, I.; Wille, H. C.; Kumar, D. Study of Interface and Its Role in an Unusual Magnetization Reversal in 57FeCoB/MgO Bilayer. *Hyperfine Interact.* **2021**, *242* (1), 4–11. <https://doi.org/10.1007/s10751-021-01736-4>.
- (13) Jamal, M. S.; Gupta, P.; Raj, R.; Gupta, M.; Reddy, V. R.; Kumar, D. Structural and Magnetic Asymmetry at the Interfaces of MgO/FeCoB/MgO Trilayer: Precise Study under x-Ray Standing Wave Conditions. *J. Appl. Phys.* **2022**, *131*, 235301. <https://doi.org/10.1063/5.0092977>.
- (14) Greer, A. A.; Gray, A. X.; Kanai, S.; Kaiser, A. M.; Ueda, S.; Yamashita, Y.; Bordel, C.; Palsson, G.; Maejima, N.; Yang, S.-H.; Conti, G.; Kobayashi, K.; Ikeda, S.; Matsukura, F.; Ohno, H.; Schneider, C. M.; Kortright, J. B.; Hellman, F.; Fadley, C. S. Observation of Boron Diffusion in an Annealed Ta/CoFeB/MgO Magnetic Tunnel Junction with Standing-Wave Hard x-Ray Photoemission. *Appl. Phys. Lett.* **2012**, *101* (20), 202402. <https://doi.org/10.1063/1.4766351>.
- (15) Read, J. C.; Mather, P. G.; Buhrman, R. A. X-Ray Photoemission Study of Co Fe B/Mg O Thin Film Bilayers. *Cit. Appl. Phys. Lett.* **2007**, *90*, 132503. <https://doi.org/10.1063/1.2717091>.
- (16) Bae, J. Y.; Lim, W. C.; Kim, H. J.; Lee, T. D.; Kim, K. W.; Kim, T. W. Compositional Change of MgO Barrier and Interface in Co Fe B/Mg O/Co Fe B Tunnel Junction after Annealing. *Cit. J. Appl. Phys.* **2006**, *99*, 8–316. <https://doi.org/10.1063/1.2170591>.

- (17) Gupta, A.; Kumar, D.; Meneghini, C. Interface Structure in Magnetic Multilayers Using X-Ray Standing Waves. *Phys. Rev. B* **2007**, *75*, 064424. <https://doi.org/10.1103/PhysRevB.75.064424>.
- (18) Li, W.; Zhu, J.; Li, H.; Zhang, Z.; Ma, X.; Yang, X.; Wang, H.; Wang, Z. Ni Layer Thickness Dependence of the Interface Structures for Ti/Ni/Ti Trilayer Studied by X-Ray Standing Waves. *ACS Appl. Mater. Interfaces* **2013**, *5* (2), 404–409. https://doi.org/10.1021/AM3024614/ASSET/IMAGES/LARGE/AM-2012-024614_0004.JPEG.
- (19) Nayak, S.; Das, S. S.; Singh, B. B.; Charlton, T. R.; Kinane, C. J.; Bedanta, S. Study of the Magnetic Interface and Its Effect in Fe/NiFe Bilayers of Alternating Order. *RSC Adv.* **2020**, *10* (56), 34266–34275. <https://doi.org/10.1039/d0ra05429a>.
- (20) Tsoy, G.; Janu, Z.; Novak, M.; Soukup, F.; Tichy, R. High-Resolution SQUID Magnetometer. *Phys. B Condens. Matter* **2000**, 284–288, 2122–2123. [https://doi.org/10.1016/S0921-4526\(99\)03023-9](https://doi.org/10.1016/S0921-4526(99)03023-9).
- (21) Kumar, D.; Gupta, A.; Patidar, P.; Banerjee, A.; Pandey, K. K.; Sant, T.; Sharma, S. M. Interface Induced Perpendicular Magnetic Anisotropy in a Co/CoO/Co Thin-Film Structure: An in Situ MOKE Investigation. *J. Phys. D. Appl. Phys.* **2014**, *47* (10). <https://doi.org/10.1088/0022-3727/47/10/105002>.
- (22) Pacyna, A. W.; Ruebenbauer, K. General Theory of a Vibrating Magnetometer with Extended Coils. *J. Phys. E.* **1984**, *17* (2), 141. <https://doi.org/10.1088/0022-3735/17/2/016>.
- (23) Won, S.; Saun, S. B.; Lee, S.; Lee, S.; Kim, K.; Han, Y. NMR Spectroscopy for Thin Films by Magnetic Resonance Force Microscopy. *Sci. Rep.* **2013**, *3*. <https://doi.org/10.1038/SREP03189>.
- (24) Gellert, R.; Geiss, O.; Klingelhöfer, G.; Ladstätter, H.; Stahl, B.; Walter, G.; Kankeleit, E. Depth Selective CEMS in the Energy Range 0 to 20 KeV. *Nucl. Instruments Methods Phys. Res. Sect. B Beam Interact. with Mater. Atoms* **1993**, *76* (1–4), 381–382. [https://doi.org/10.1016/0168-583X\(93\)95246-2](https://doi.org/10.1016/0168-583X(93)95246-2).
- (25) Couet, S.; Schlage, K.; Diederich, T.; Rüffer, R.; Theis-Bröhl, K.; Toperverg, B. P.; Zhernenkov, K.; Zabel, H.; Röhlberger, R. The Magnetic Structure of Coupled Fe/FeO Multilayers Revealed by Nuclear Resonant and Neutron Scattering Methods. *New J. Phys.* **2009**, *11* (13pp), 13038. <https://doi.org/10.1088/1367-2630/11/1/013038>.
- (26) Oko, M.; Harada, I.; Okada, K. Theory of XAS and XMCD for the Field-Controlled Valence Mixed State in RE Compounds. <https://doi.org/10.1088/1742-6596/190/1/012016>.
- (27) Khanderao, A. G.; Sergueev, I.; Wille, H. C.; Kumar, D. Interface Resolved Magnetism at Metal-Organic (Fe/Alq₃) Interfaces under x-Ray Standing Wave Condition. *Appl. Phys. Lett.* **2020**, *116* (10). <https://doi.org/10.1063/1.5135361>.
- (28) Andreeva, M. A.; Lindgren, B. Nuclear Resonant Spectroscopy at Bragg Reflections from Periodic Multilayers: Basic Effects and Applications. *PRB* **2005**, *72*, 125422.

<https://doi.org/10.1103/PhysRevB.72.125422>.

- (29) Niesen, L.; Mugarza, A.; Rosu, M. F.; Coehoorn, R.; Jungblut, R. M.; Roozeboom, F.; Baron, A. Q. R.; Chumakov, A. I.; Rü, R. Magnetic Behavior of Probe Layers of 57 Fe in Thin Fe Films Observed by Means of Nuclear Resonant Scattering of Synchrotron Radiation. **1998**.
- (30) Liu, Y.; Watson, S. M.; Lee, T.; Gorham, J. M.; Katz, H. E.; Borchers, J. A.; Fairbrother, H. D.; Reich, D. H. Correlation between Microstructure and Magnetotransport in Organic Semiconductor Spin-Valve Structures. <https://doi.org/10.1103/PhysRevB.79.075312>.
- (31) Rohlsberger, R. *Nuclear Condensed Matter Physics with Synchrotron Radiation*; Springer, 2003; Vol. 208.
- (32) Andreeva, M.; Smekhova, A.; Baulin, R.; Repchenko, Y.; Bali, R.; Schmitz-Antoniak, C.; Wende, H.; Sergueev, I.; Schlage, K.; Wille, H.-C. Evolution of the Magnetic Hyperfine Field Profiles in an Ion-Irradiated Fe₆₀Al₄₀ Film Measured by Nuclear Resonant Reflectivity. *J. Synchrotron Radiation* **2021**, *28* (5). <https://doi.org/10.1107/S1600577521007694>.
- (33) Merkel, D. G.; Hegedüs, G.; Gracheva, M.; Deák, A.; Illés, L.; Németh, A.; Maccari, F.; Radulov, I.; Major, M.; Chumakov, A. I.; Bessas, D.; Nagy, D. L.; Zolnai, Z.; Graning, S.; Sájerman, K.; Szilágyi, E.; Lengyel, A. A Three-Dimensional Analysis of Magnetic Nanopattern Formation in FeRh Thin Films on MgO Substrates: Implications for Spintronic Devices. *ACS Appl. Nano Mater.* **2022**, *5* (4), 5516–5526. <https://doi.org/10.1021/ACSANM.2C00511>/ASSET/IMAGES/LARGE/AN2C00511_0011.JPEG.
- (34) Parratt, L. G. Surface Studies of Solids by Total Reflection of X-Rays. *Phys. Rev.* **1954**, *95* (2), 359–369. <https://doi.org/10.1103/PhysRev.95.359>.
- (35) Londhe, V. P.; Gupta, A.; Ponpandian, N.; Kumar, D. TiO₂ as Diffusion Barrier at Co / Alq₃ Interface Studied by x-Ray Standing Wave Technique. *J. Phys. D. Appl. Phys.* **2018**, *51*, 225303. <https://doi.org/10.1088/1361-6463/aabf7a>.
- (36) Kumar, D.; Gupta, A. Interface Study of Ag/57Fe/Ag Trilayer Using Mössbauer and X-Ray Standing Wave Analysis. *Hyperfine Interact.* **2008**, *185* (1–3), 29–32. <https://doi.org/10.1007/s10751-008-9808-4>.
- (37) Kumar, D.; Gupta, P.; Gupta, A. In Situ Surface Magneto-Optical Kerr Effect (s-MOKE) Study of Ultrathin Soft Magnetic FeCuNbSiB Alloy Films. *Mater. Res. Express* **2015**, *1* (4). <https://doi.org/10.1088/2053-1591/1/4/046405>.
- (38) Qiao, X.; Wang, B.; Tang, Z.; Shen, Y.; Yang, H.; Wang, J.; Zhan, Q.; Mao, S.; Xu, X.; Li, R. W. Tuning Magnetic Anisotropy of Amorphous CoFeB Film by Depositing on Convex Flexible Substrates. *AIP Adv.* **2016**, *6* (5), 056106. <https://doi.org/10.1063/1.4943153>.
- (39) Stoner, E. C.; F. R. S.; and Wohlfarth, E. P. A Mechanism of Magnetic Hysteresis in Heterogeneous Alloys. **1948**, *826* (May).

- (40) Reich, S.; Shtrikman, S. Angular Variation of Coercivity in Orthoferrite Single Crystals. **1965**, *567* (1962), 140–141. <https://doi.org/https://doi.org/10.1063/1.1713860>.
- (41) Suponev, N. P.; Grechishkin, R. M.; Lyakhova, M. B.; Pushkar, Y. E. Angular Dependence of Coercive Field in (Sm,Zr) (Co,Cu,Fe)_z Alloys. *J. Magn. Magn. Mater.* **1996**, *157–158*, 376–377. [https://doi.org/10.1016/0304-8853\(95\)00992-2](https://doi.org/10.1016/0304-8853(95)00992-2).
- (42) Hussain, Z.; Reddy, V. R.; Kumar, D.; Ganesan, V.; Dhamgaye, V.; Khantwal, N.; Gupta, A. Study of Two Phase Magnetization Reversal in Patterned Cobalt Thin Film. *J. Phys. D. Appl. Phys.* **2017**, *50*, 425001. <https://doi.org/10.1088/1361-6463/aa8524>.
- (43) Mathews, M.; Houwman, E. P.; Boschker, H.; Rijnders, G.; Blank, D. H. A. Magnetization Reversal Mechanism in La_{0.67}Sr_{0.33}MnO₃ Thin Films on NdGaO₃ Substrates. *J. Appl. Phys.* **2010**, *107* (1). <https://doi.org/10.1063/1.3273409>.
- (44) Barwal, V.; Husain, S.; Behera, N.; Goyat, E.; Chaudhary, S. Growth Dependent Magnetization Reversal in Co₂MnAl Full Heusler Alloy Thin Films. *Cit. J. Appl. Phys.* **2018**, *123*, 53901. <https://doi.org/10.1063/1.5004425>.
- (45) Andreeva, M. A.; Baulin, R. A.; Repchenko, Y. L. Standing Wave Approach in the Theory of X-Ray Magnetic Reflectivity. *J. Synchrotron Radiat.* **2019**, *26* (2), 483–496. <https://doi.org/10.1107/S1600577518018398>.
- (46) Andreeva, M. A. Nuclear Resonant Reflectivity Data Evaluation with the “REFTIM” Program. *Hyperfine Interact* **2008**, *185*, 17–21. <https://doi.org/10.1007/s10751-008-9806-6>.
- (47) E Johnson, B. C.; Ridout, M. S.; Cranshaw, T. E. The Mossbauer Effect in Iron Alloys. **1963**, *81*.
- (48) Klein, H.-P.; Ghafari, M.; Ackermann, M.; Gonser, U.; Wagner, H.-G. CRYSTALLIZATION OF AMORPHOUS METALS. *Nucl. Instruments Methods* **1982**, *199*, 159–162.
- (49) Ghafari, M.; Peng, G.; Wang, D.; Imai, Y.; Kamali, S. Occurrence of Two Amorphous Phases in an Fe₄₀Co₄₀B₂₀ Alloy. *Mater. Lett.* **2016**, *164*, 535–538. <https://doi.org/10.1016/J.MATLET.2015.10.098>.
- (50) Burton, J. D.; Jaswal, S. S.; Tsymbal, E. Y.; Mryasov, O. N.; Heinonen, O. G. Atomic and Electronic Structure of the CoFeB / MgO Interface from First Principles. **2006**. <https://doi.org/10.1063/1.2360189>.
- (51) Harnchana, V.; Hindmarch, A. T.; Sarahan, M. C.; Marrows, C. H.; Brown, A. P.; Brydson, R. M. D. Evidence for Boron Diffusion into Sub-Stoichiometric MgO (001) Barriers in CoFeB/MgO-Based Magnetic Tunnel Junctions. *J. Appl. Phys.* **2013**, *113* (16). <https://doi.org/10.1063/1.4802692>.
- (52) Cha, J. J.; Read, J. C.; Buhrman, R. A.; Muller, D. A. Spatially Resolved Electron Energy-Loss Spectroscopy of Electron-Beam Grown and Sputtered CoFeBMgOCoFeB Magnetic Tunnel Junctions. *Appl. Phys. Lett.* **2007**, *91* (6). <https://doi.org/10.1063/1.2769753>.

- (53) Kumar, D.; Singh, S.; Vishwakarma, P.; Dev, A. S.; Reddy, V. R.; Gupta, A. Tailoring of In-Plane Magnetic Anisotropy in Polycrystalline Cobalt Thin Films by External Stress. *J. Magn. Magn. Mater.* **2016**, *418*, 99–106. <https://doi.org/10.1016/J.JMMM.2016.03.072>.
- (54) Dev, A. S.; Kumar, D.; Gupta, P.; Vishwakarma, P.; Gupta, A. Development of Residual Stress and Uniaxial Magnetic Anisotropy during Growth of Polycrystalline Co Film. *Mater. Res. Bull.* **2020**, *121*, 110616. <https://doi.org/10.1016/J.MATERRESBULL.2019.110616>.